

# Numerical Modeling of the Excimer Beam

Ying Lin\* and Jesse Buck

Cymer, Inc., Mail Stop 2-2A, 16710 Via Del Campo, San Diego, CA 92127

## ABSTRACT

Using detailed metrology and modeling, the excimer beam may be completely characterized making it possible to achieve good agreement among various test methods and allowing accurate prediction of the beam performance in photolithographic and other applications. Full characterization consists of determining the intensity envelope, wavefront error, and detailed speckle structure statistics. The numerical model consists of a series of exact two-dimensional instantaneous representations of the complex amplitude propagated through the beam train, with time varying speckled structure and integration to generate the time-averaged beam envelope. The detailed description provides a means to validate simpler, but more approximate, theories and to determine the limits of accuracy of these simpler methods for various experiment configurations. We also show results of very recent time-resolved experiments of near-field and focal plane profiles.

## 1. INTRODUCTION

The excimer beam has both high brightness and limited spatial and temporal coherence which makes it an excellent source for photolithography. While the time-integrated envelope of the excimer beam exhibits a smooth profile, its propagation behavior and performance in photolithographic systems and other applications cannot be described without an understanding of the underlying instantaneous speckled behavior. When observed on an instantaneous basis, the excimer beam will appear to be a speckled structure as illustrated schematically in Fig. 1.

The speckled structure changes rapidly with a time constant inversely related to the spectral width of the excimer beam. In photolithographic application, the time required for the speckles to change is typically several orders of magnitude less than the exposure time, so that the speckles average out almost completely yielding a smooth overall envelope. In this paper we report time-averaged experiments and calculations which are predictive of time-averaged photolithographic applications. We also report preliminary results of time-resolved experiments to observe beam properties on nanosecond time scales.

A fly's eye homogenizer is often used to transform the nonuniform envelope of the excimer beam into a highly uniform distribution (see Fig. 2)<sup>1-2</sup>. This results from the fact that while the distribution over the full aperture of the fly's eye array may be nonuniform, the distribution is considerably flatter when the beamlets are overlapped. The reduction in nonuniformity obeys approximately the  $1/\sqrt{N}$  rule where  $N$  is the number of elements in the fly's eye lens. However, for this averaging to occur, the distribution from the various lens elements must be mutually incoherent, which implies that the speckle size must be less than the diameter of the lens elements. If the speckle size is not sufficiently small, artifacts due to coherent interference effects between neighboring lenslets will degrade the uniformity of the illumination at the plane of the photolithographic mask.

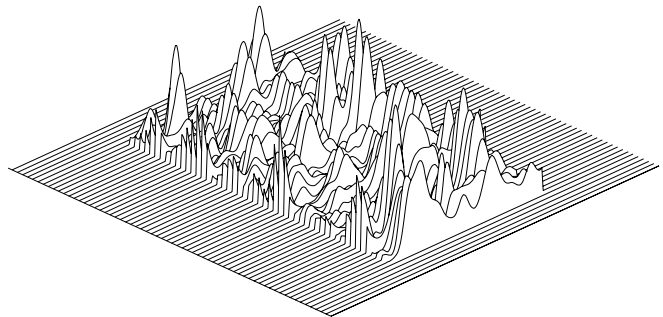


Fig. 1. The excimer beam exhibits a speckled structure when viewed instantaneously.

\*Correspondence: Email: ylin@cymer.com; <http://www.cymer.com>; Tel: 619 618 5221, Fax: 619 618 3048

A variety of tests have been employed to characterize speckle size and shape including Young's double hole and Moire interferometry<sup>3-6</sup>. It is commonly assumed that speckle statistics are the same in all regions of the aperture (stationary statistics). We shall show later in this paper that this is not strictly true for the excimer beam. However we begin our discussion with the familiar stationary model.

For stationary statistics, the statistical size and shape of the speckle is commonly characterized by the time-averaged autocorrelation function:

$$R(\Delta x, \Delta y) = \langle \iint p^* \left( x + \frac{\Delta x}{2}, y + \frac{\Delta y}{2} \right) p \left( x - \frac{\Delta x}{2}, y - \frac{\Delta y}{2} \right) dx dy \rangle \quad (1)$$

where  $p(x,y)$  is the instantaneous complex amplitude and  $\langle \rangle$  denotes an average over time<sup>7</sup>. We can also determine the speckle size indirectly by the measurements of beam diameter in the far-field of the lens. We may relate the averaged irradiance in the far-field to the autocorrelation function<sup>8</sup>:

$$R(x, y) = \iint_{-\infty}^{\infty} I(x', y') e^{j \frac{2\pi}{\lambda f} (xx' + yy')} dx' dy' \quad (2)$$

where  $I(x', y')$  is the far-field irradiance.

The autocorrelation function defines the speckle size in a given plane, but the speckle size and angular divergence change as the beam propagates. Figure 3 illustrates the fact that, as the beam expands with diffraction propagation, the speckle size (and the associated autocorrelation size) increases and the angular divergence decreases. Measurements taken at different planes will not agree. Similarly if the plane of characterization is not the plane which is actually imaged onto the flies eye homogenizer, the measurement will not accurately reflect the actual performance in the application.

In principle, we can measure the speckle size indirectly by measuring the beam width in the far-field of the beam after the lens to determine the angular divergence and the Fourier transform relationship of Eq. (1) to determine the autocorrelation size<sup>9</sup>. While this may seem simple it is, in fact, rather difficult to locate the far-field point accurately. The plane of the output coupler has a significant phase radius of curvature because of propagation from the internal waist (see Fig. 3). This phase radius, the distance of the test plane from the lens, and the focal length of the lens may be used with the Lens Law to determine the true far field point  $S'$  (see Fig. 4). One must then measure the beam profile at  $S'$  and divide by the conjugate

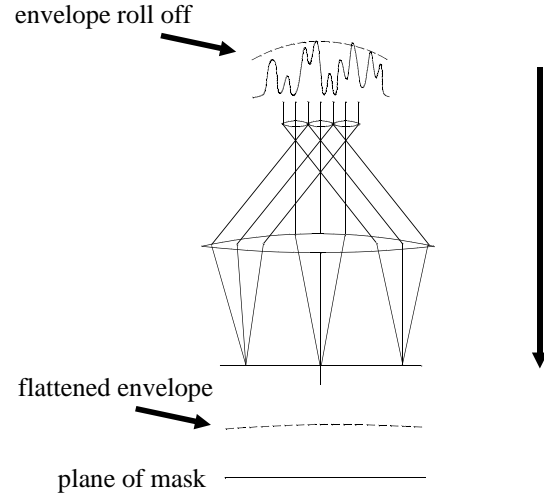


Fig. 2. The flies eye homogenizer cuts out small sections of the beam, expands them, and overlaps the sections to smooth out the envelope at the plane of the photolithographic mask. The speckles should be smaller than the diameter of the flies eye lenses elements to avoid coherent interference between lenslet images that would create fringes in the plane of the mask.

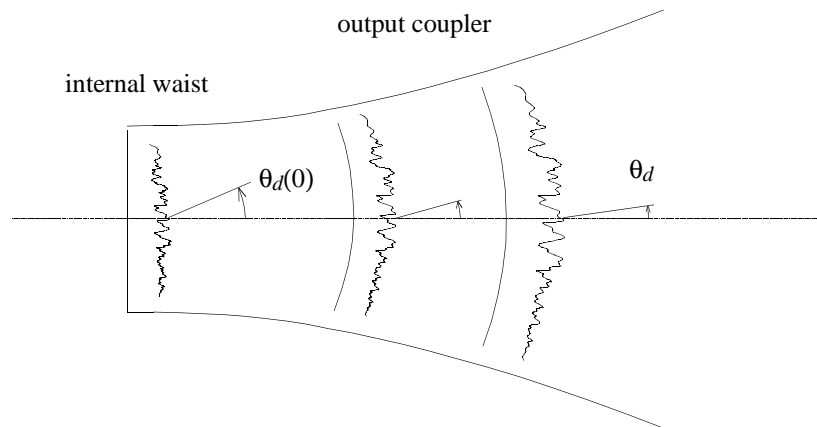


Fig. 3. The divergence due to speckle decreases as the beam expands. Maximum divergence exists at the internal waist of the laser.

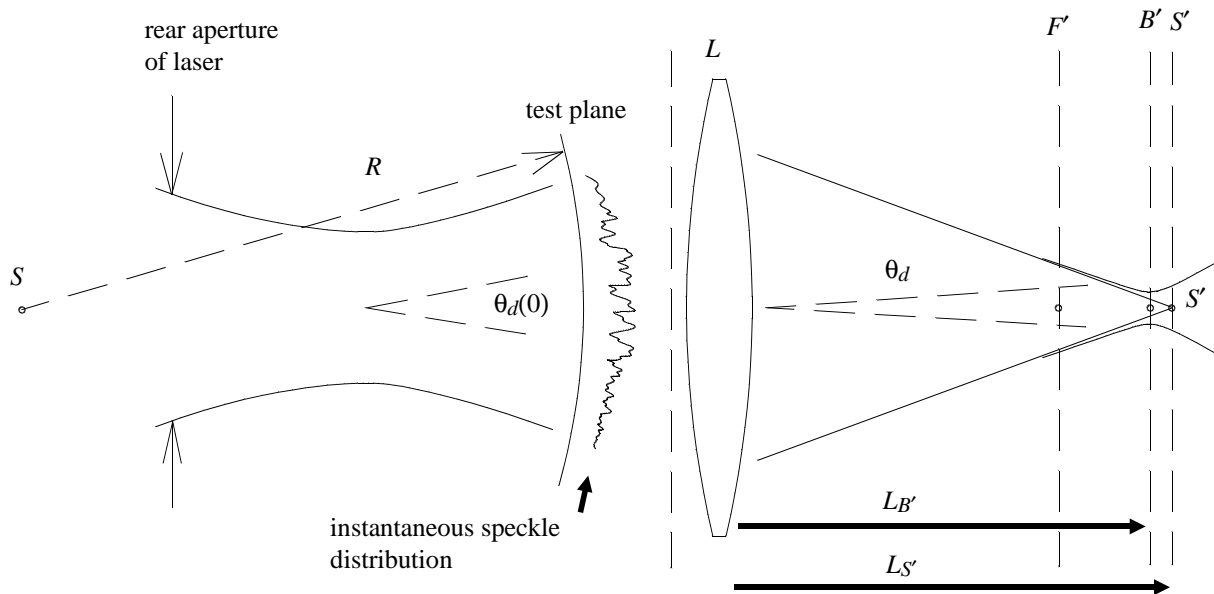


Fig. 4. An instantaneous speckle distribution with a radius of curvature  $R$  and a center of the wavefront radius at  $S$  is shown at the test plane. For testing, the test plane is often placed close to an objective lens with rear focal point  $F'$ . The divergence  $\theta_d$  due to speckle defines the beam size in the far field, at the geometric image of  $S$  located at  $S'$ . The point of minimum blur at  $B'$  lies inside of  $S'$  — on the lens side of the geometric focus.

The beam may be characterized by scanning a knife edge or slit across the beam. The scanned profile and axial position of  $S'$  provides direct information on the divergence  $\theta_d$  at the test plane. The scanned profile at position  $F'$  provides direct information on the intrinsic divergence  $\theta_d(0)$  of the internal waist of the laser. Combinations of scans may be combined with diffraction theory to calculate a comprehensive solution.

The rear aperture of the laser does some clipping of the beam. This aperture is imaged by the test lens to the far side of the focus region and affects the through-focus beam widths in this region (See Fig. 12).

distance  $L_{S'}$  to get the angular divergence  $\theta_d$  at the test plane. In practice the beam width measurement is often made at the plane of minimum blur  $B'$  because this point is more easily located and the divergence calculated by dividing by  $L_{B'}$ , the distance from the lens to the plane of minimum blur. Use of minimum blur data in this way can lead to a significant error, especially if a relatively long focal length lens is used so that  $B'$  and  $S'$  are well separated.

### 1.1. Full characterization of the excimer beam

A coherent beam may be fully characterized by the intensity profile and the wavefront distribution at a plane (Fig. 5a)<sup>10-11</sup>. To fully characterize the partially coherent excimer beam we must add a description of the speckle statistics to the description of intensity and wavefront distributions.

Given the full state of the partially coherent beam, we can calculate the detailed beam properties at any plane, albeit with substantial calculation effort. We

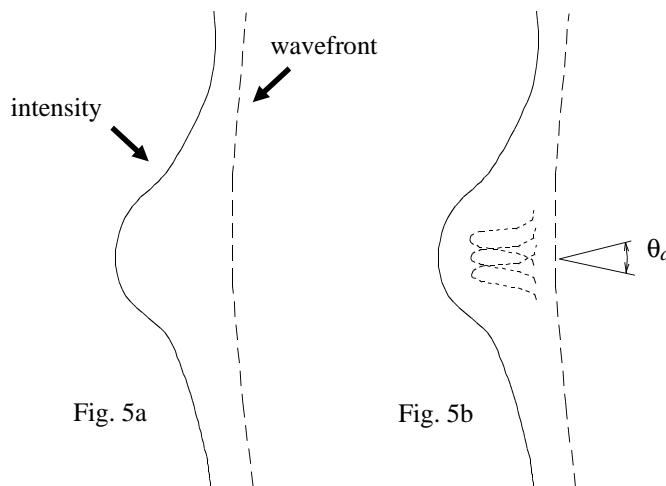


Fig 5a. The fully coherent beam may be characterized by the intensity and wavefront distribution. Fig 5b. The partially coherent beam requires characterization of the speckle distribution (and diffraction angle  $\theta_d$ ) in addition to the intensity and wavefront distribution.

can also accurately predict the values that would be measured by any of the common tests or any test that we might devise.

Conversely we can solve the inverse problem of fitting the free variables that define the parameters of the system to a collection of experimentally determined parameters.

### 1.2. Simulation of the partially coherent excimer beam

We can simulate the partially coherent beam by constructing a series of instantaneous representations of the beam, each with the correct intensity and wavefront distributions and a speckle structure constructed to have the proper statistical shape and width. Each instance is represented as a square complex amplitude array of dimensions from  $256 \times 256$  to  $2048 \times 2048$  points. To determine the beam characteristics at some other plane, we perform diffraction propagation of each instance array and sum the instantaneous distributions incoherently. A minimum of several hundred arrays must be averaged to yield the smooth envelope exhibited by the excimer beam. The procedure exactly emulates the actual physical process and requires only Fresnel diffraction which is both well understood and numerically convenient, so we may be confident of the accuracy of the procedure.

### 1.3 Partially coherent description by number of modes and $M^2$

The difficulty of the calculations depends on the typical number of speckles across the diameter of the beam. The number of speckles across the beam diameter is approximately the same as the  $M^2$  value<sup>12-13</sup>. For excimer beams there may be a broad range of  $M^2$  values. Typical values of  $M^2$  may range from fewer than 10 to more than 100. As we need at least 6 to 8 sample points per speckle and some guardband surrounding the distribution, computer arrays of from  $256 \times 256$  to  $2048 \times 2048$  may be required. With a contemporary PC computer we can model even complex system in times ranging from a few minutes to several hours<sup>14</sup>. We used a commercial computer program called GLAD, which enabled us to build a numerical model consisting of diffraction propagation, apertures, lenses, interference effects and other elements of the system<sup>15</sup>.

### 1.4 Example of through-focus propagation

Consider the straightforward case of gaussian envelope and gaussian-shaped speckle. We may calculate the through-focus performance by propagating through a series of short steps through the focus region. Fig. 6a shows a series of profiles of

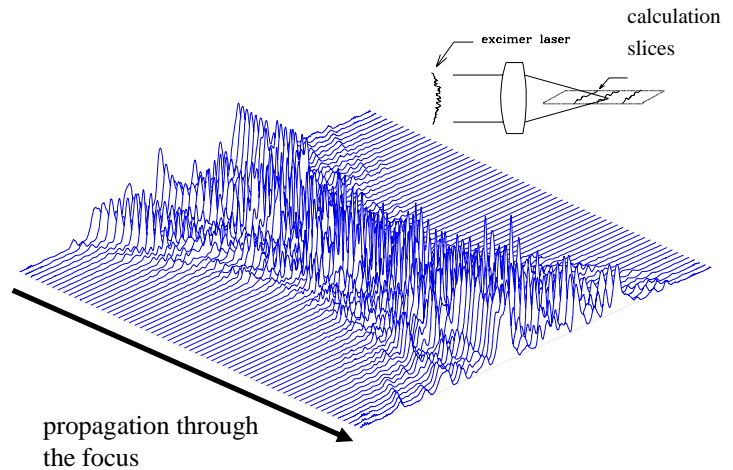


Fig. 6a. Propagation of an instantaneous speckle distribution of the excimer laser through focus from the lens side (upper left) to beyond focus (lower right). The figure shows profiles through the beam made by a series of scans across the

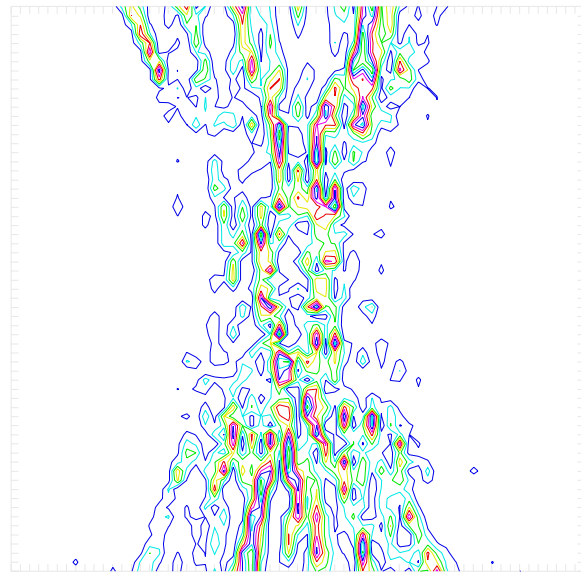


Fig. 6b. Propagation of an instantaneous speckle distribution. Same as Fig. 6a with contours.

intensity taken at 64 steps through the focus region for a single instance of speckle. Fig. 6b shows a contour plot through the same region. Each diagonal slice has been peak-normalized to better show the change in beam diameter. Even with a single instance we can see the gaussian-like behavior of the envelope of the beam as it necks down to form a waist and expands again. Note also that the size of the speckles expands with the overall width so that the number of speckles across the width remains relatively constant (at the  $M^2$  value). Note also that the longitudinal length of the speckles is much larger in the expanded parts of the beam. Figs. 7a and 7b show the through-focus behavior if the same gaussian envelope with gaussian-shaped speckle with very long averaging.

A beam that has both a gaussian envelope and gaussian-shaped speckle is frequently called a gaussian-Schell beam. The envelope of the gaussian-Schell beam has the same behavior as a true gaussian beam with the same waist radius and an equivalent wavelength equal to  $\lambda_{eff} = M^2\lambda$ .

Strict gaussian-Schell behavior requires both a gaussian envelope and gaussian-shaped speckle, but these conditions are rarely satisfied exactly in real excimer laser beams because of apertures clipping. (Recent time-resolved results presented in Section 3 suggest that dynamic changes in the laser during a pulse may contribute to nonstationary statistics.) Figs. 8a and 8b show the through focus behavior for an initially gaussian beam that has been strongly clipped. This beam is averaged only 400 times and we see some residual irregularity due to the incomplete averaging. We also note a departure from gaussian-like behavior — most obviously, the shape changes through focus.

## 2. VALIDATION OF THE NUMERICAL MODELING METHOD FOR A TYPICAL TEST CONFIGURATION

Consider a representative test configuration shown in Fig. 4. The intensity profile and wavefront distribution are to be measured in detail at the test plane at the lens and the beam width is to be measured at one or more predefined planes in the vicinity of the waist, perhaps at the rear focal plane  $F'$  and one or more other planes. For production testing it is much more convenient to make scans at predefined plans rather than to search for the plane of minimum blur or some other special condition. We want to test the suitability of our numerical model to determine: 1) the accuracy that we may expect to achieve with certain levels of precision in the measurement and 2) the number and location of the predefined axial scan positions.

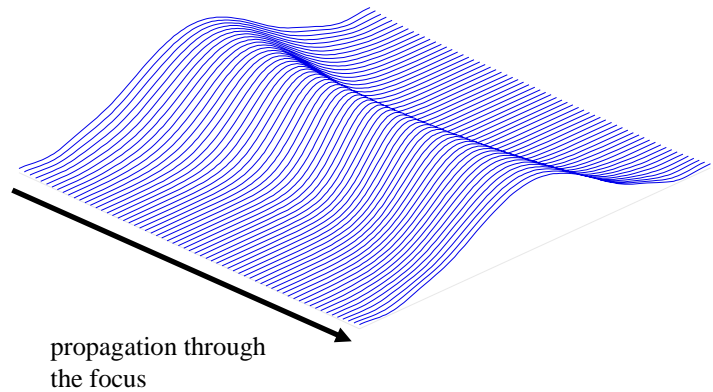


Fig. 7a. Time-average of the propagation of an instantaneous speckle distribution of the excimer laser through focus from the lens side (upper left) to beyond focus (lower right). The figure shows profiles through the beam made by a series of scans across the diameter of the beam. Each diagonal slice is peak-normalized to the same value to show the beam widths more clearly. The gaussian-like behavior is clear.

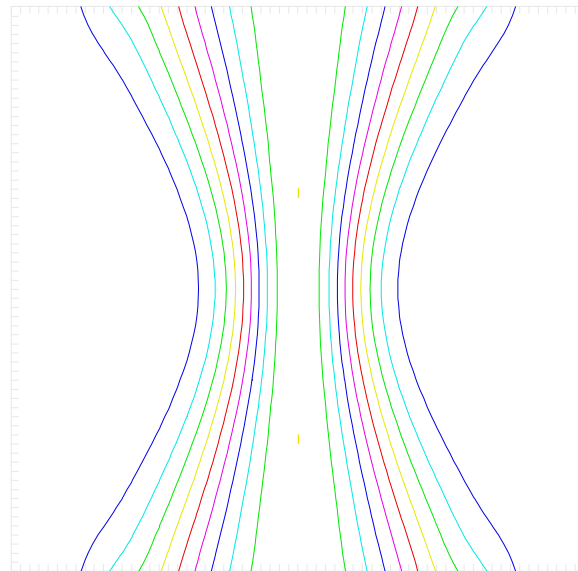


Fig. 7b. Time-average of the propagation of an instantaneous speckle distribution. Same as Fig 7a with contours. Gaussian behavior is clear.

To test the suitability of our numerical modeling methods on this type of configuration, we performed experiments on a "lab" laser (performance is not necessarily the same as production Cymer lasers). We measured the intensity and wavefront profiles with high sampling density in a plane near an objective lens and performed multiple scans in the focused region following lens.

The intensity distribution was obtained by scanning a slit aperture over the distribution at the test plane. Fig. 9, shows an intensity profile representing a scan of the slit in the horizontal direction. Excimer lasers typically have different behavior in two planes of symmetry. For simplicity in this paper we shall consider only the horizontal direction. While this distribution in Fig. 9 is roughly gaussian it is not exactly so and the difference is enough to be significant.

The wavefront slope across the beam was measured by a Hartmann test consisting of scanning a slit across the beam and observing the shift in centroid of the beam at the focal plane of a 1 meter lens. Fig. 11 shows the Hartmann test schematically. Fig. 10 shows a typical trace of beam centroid vs. the center of the scanned aperture, yielding the wavefront slope vs. aperture position. Integrating the wavefront slope yields the wavefront. The radius was measured to be -374 cm at the test plane. A constant wavefront slope indicates defocus, i.e., phase radius of curvature and the slight 3rd order behavior indicates a small amount of spherical aberration. The defocus is a natural characteristic of the expanding partially coherent beam.

A lens of 1 meter radius was used to form a focused beam from the excimer laser. A simplified schematic of the laser resonator and objective lens is shown in Fig. 4. The rear aperture of the laser plays an important role in clipping the beam and ultimately defining the beam properties. The test plane was placed at the front of the objective lens. The far-field at  $S'$  is calculated to be approximately 36.5 cm beyond the rear focal plane at  $F'$ . Figure 12 displays a set of widths of the beam at 50%, 36%, 14%, and 5% intensity points for seven axial positions, giving us a total of 28 data points. Figure 12 clearly shows that the shape of the beam changes substantially in propagating through the focus region and that the beam shape is quite different on either side of focus.

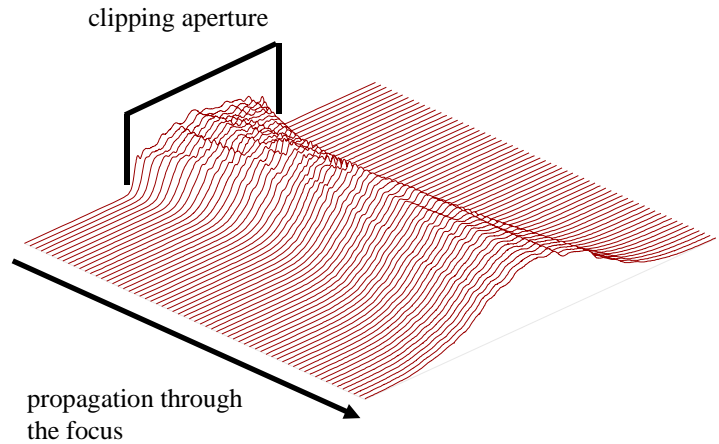


Fig. 8a. Partial complete time-average of clipped speckle distribution. Averaging was done over 400 time steps, so the speckle structure is not completely averaged out. Gaussian-like behavior resumes a short distance from the clipping aperture.

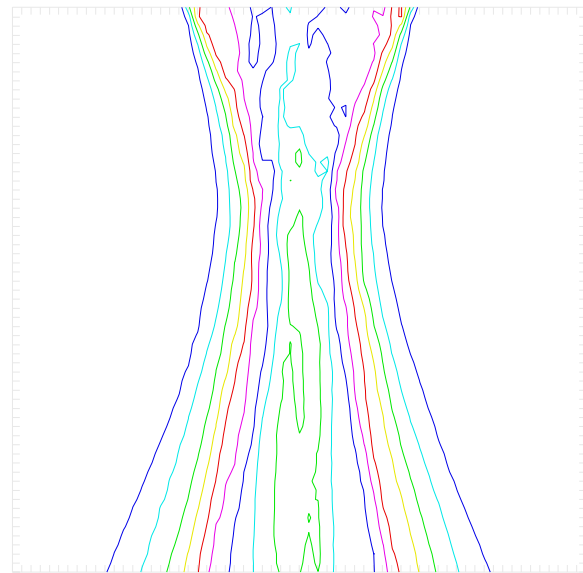


Fig. 8b. Partial complete time-average of clipped speckle distribution. Averaging was done over 400 time steps, so the speckle structure is not completely averaged out.

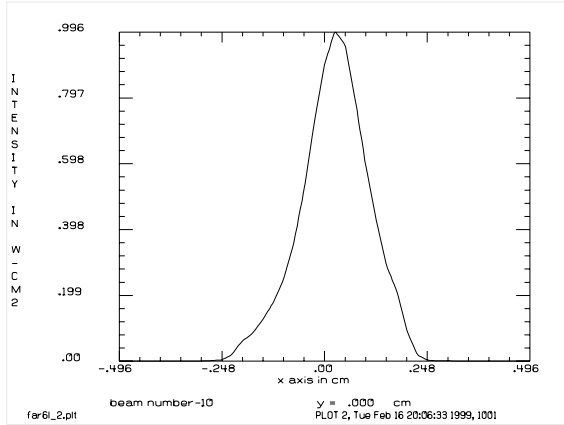


Fig. 9. Profile of intensity of one specific excimer beam along the horizontal direction. Profile is somewhat gaussian-like but the departure from gaussian behavior is observable in the through-focus data.

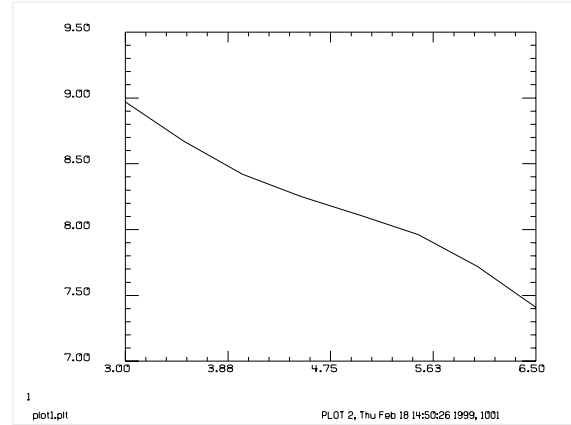


Fig. 10. Trace of wavefront slope across the aperture in the horizontal direction as measured by a Hartmann test. Slope indicates defocus; cubic term indicates spherical aberration.

## 2.1 Uniqueness of the solution

The issue of uniqueness of the solution must be considered in any optimization or data fitting. We believe that the solution for speckle size and shape is unique, so that any method of optimization (even trial and error) that results in a good match to the data has to be the correct solution, within the limits of uncertainty of the data and the finite number of data points.

## 2.2 Fitting with a single-plane model and gaussian-shaped speckle

We first consider how well we can fit the through-focus data using the intensity distribution measured at the lens (Fig. 9) and the phase radius of curvature combined with stationary, gaussian speckle statistics, i.e., the speckle has the same statistical gaussian shape and width at all points in the aperture.

We used the data of Figure 12 as targets in a least squares optimization procedure. Figure 13 shows the result of optimization to fit the through-focus data by assuming gaussian speckle and simply varying the speckle size. With this single variable we can not get the strong differentiation on the two sides of the waist.

## 2.3 Conditioning the speckle statistics with a simplified resonator model

To improve the model, we included the simplified form of the resonator shown in Fig. 4. The rear aperture is known to clip the edges of the beam. This effect can alter the gaussian shape of statistics to generate nongaussian shapes and cause the speckle size to vary over the aperture, i.e., breaking the stationarity of the statistics, similar to that shown in Figs. 8a and 8b.

To include the effects of the rear aperture, we began with gaussian speckle at the plane of the lens and then back propagated to the plane of the rear aperture (or equivalently we could forward propagate to the image of the rear aperture as formed by the 1 meter lens). The beam is then lightly trimmed by the rear aperture and then propagated back to the lens.

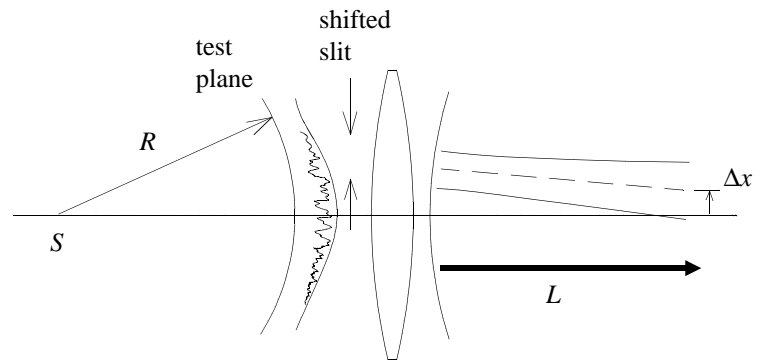


Fig. 11. The radius of the beam may be observed by shifting a small (but finite) sized aperture across the aperture. The centroid of the light through the shifted slit establishes the direction of normals to the wavefront. The displacement of the beam  $\Delta x$  gives the local wavefront slope as indicated in Fig. 10.

The returned wavefront is slightly changed by the trimming effect of the aperture. We have already seen in Figs. 8a and 8b the change in envelope created by relatively strong clipping. Note that the waist is shifted more toward the clipping aperture and the expansion of the beam after the waist differs from the strictly gaussian profiles of Figs. 7a and 7b. We, therefore expect at least some change in radius of curvature due to our clipping. It is necessary to compensate for this effect in the numerical model so that the phase radius of curvature of the clipped beam in the numerical model matches the experimentally measured value of -374 cm.

In numerical modeling as in experiments, we cannot observe the wavefront directly for partially coherent beams. Figure 15 shows the time-integrated interference pattern formed between the state of the beam before and after rear aperture trimming. Numerically, we simply save the starting beam, perform the propagation and trimming at the rear aperture, and then coherently add the return beam to the saved, starting beam producing an instantaneous interference pattern. Hundreds of instantaneous interference patterns are averaged to build the noise-reduced interferogram of Figure 15. The interferogram indicates an error of nearly pure defocus of about 5.75 waves at the .2 cm radius point, at the edge of the  $.4 \times .4$  region displayed. We verified that the interference effects could be precisely canceled by 5.75 waves of defocus leaving a null fringe. The slight change in phase radius of curvature due to including rear aperture effects, is compensated in the numerical model.

Figure 14 shows the results of numerical calculation including the effects of the rear aperture. We see that the asymmetry about the waist is achieved, matching Fig. 12 better. Most of the systematic error has been removed by including the effect of the rear aperture.

To identify the specific effects on the speckle distribution introduced by the rear aperture, we compared the autocorrelation function of the speckle before and after rear-aperture clipping. Fig. 16 shows side structure at a low intensity level in the autocorrelation function due to rear-aperture clipping. Although the speckle is created initially to be gaussian for an infinite transverse field, the finite envelope changes the shape of the autocorrelation function to be nongaussian in the wings of the autocorrelation function. The effect of the rear aperture is to further alter the speckle shape. We also examined the speckle in a 0.2 cm diameter aperture in the center of the lens plane and with 0.2 cm decentering of the aperture. We see that the speckle size is slightly larger in the outer part of the beam due to rear-aperture clipping (see Fig. 17).

### **3. TIME-RESOLVED EXCIMER PULSE MEASUREMENTS**

In this section we report some very recent experiments to measure the time-resolved structure of the beam. Fig. 18 shows a schematic of the test configuration. We placed a motorized slit in front of a high speed detector. We observed the temporal pulse profiles over an approximately 64 nanosecond span for a series of transverse slit positions. The results are shown in Fig. 19. An interesting two-step pulse structure is evident. Figs. 20 and 21 show contour plots of the irradiance profiles vs. time for the near field and at the focal plane of the 1 meter test lens. The first step of the pulse is wider in the near-field and exhibits higher divergence than the second step.

### **4. CONCLUSIONS**

Direct modeling of the excimer beam with instantaneous speckle and time-averaging is demonstrated to be an effective tool for describing beam propagation and experimental observations. At least for the single horizontal axis described in this paper, stationary gaussian statistics only partially explain the through-focus behavior observed experimentally. The fit to the through-focus data is improved by including the nonstationary speckle statistics due to trimming effects of the rear aperture in a simplified model of the resonator clipping aperture.

Recent time-resolved measurements of beam parameters show interesting, complex behavior in the near-field and focal plane of the lens. Future work will extend the numerical model to include time-resolved effects.

### **REFERENCES**

1. K. A. Valiev, L. V. Velikov, G. S. Volkov and D. Yu. Zaroslov, " The optimization of excimer lasers radiation characteristics for projection lithography," Proc. of 1989 Inter. Symp. on MicroProcess Conference, 37-42 (1989).

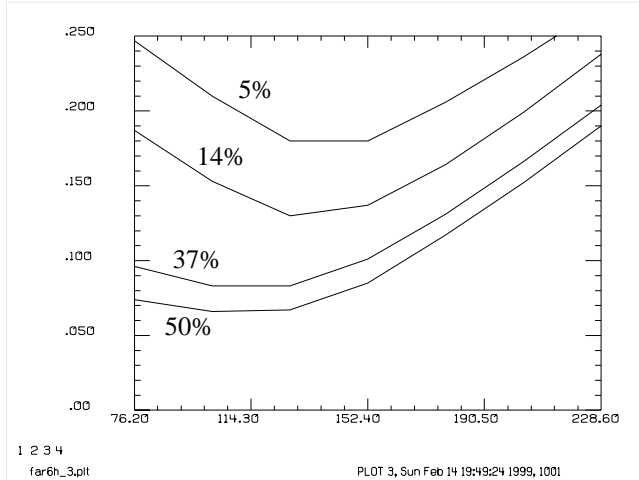


Fig. 12. Trace of beam widths for relative intensity levels of 50%, 37%, 14%, and 5% from 76.2 cm to 228.6 cm. From wavefront data the far-field point is at 136.5 cm. The shape changes from the lens-side (left) through the focus. The image of the rear aperture of the laser is imaged by the lens to a position at about 258 cm to the right of the lens causing the beam to become more square on the right side of focus.

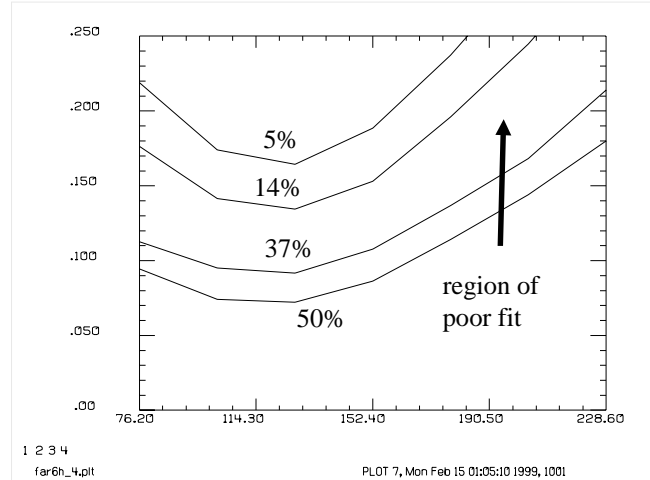


Fig. 13. Fit generated by numerical model without consideration of image of rear aperture of laser. The far side of the lens (right) is less square than in the experimental data in Fig. 12.

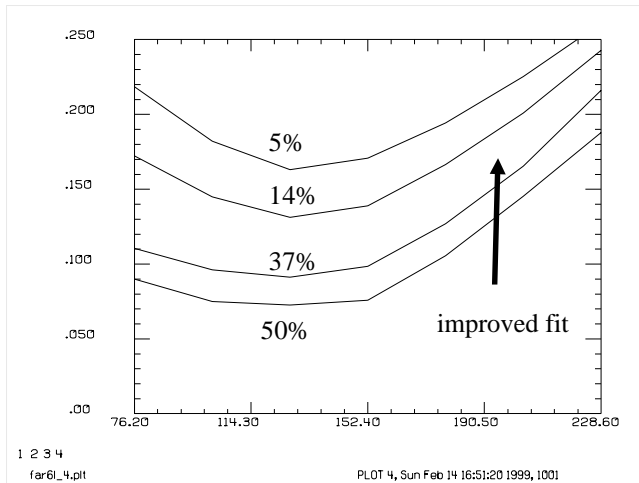


Fig. 14. Numerical fit augmented by including the rear aperture of the laser in the model.

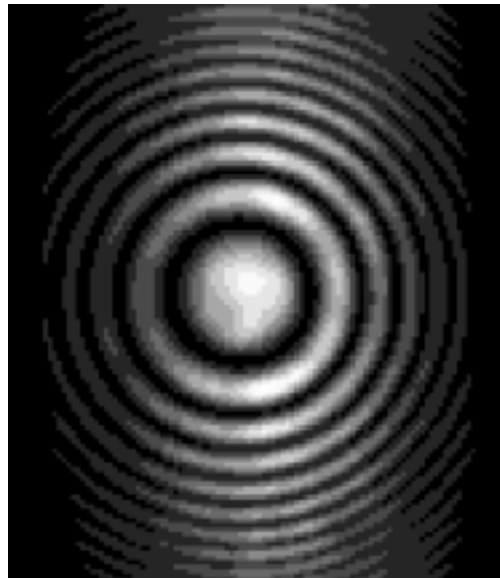


Fig. 15. Numerically generated interferogram formed between the initial distribution formed at the lens with the distribution after trimming by the rear aperture to test the change in the wavefront for a  $.4 \times .4$  cm region. The numerical interferogram shown is the time-average of hundreds of the instantaneous interferograms formed between the instantaneous speckle patterns before and after trimming by the rear aperture. The approximately 5.75 waves of defocus at the 0.2 cm radius point in the aperture represent a slight defocus which is compensated for in the model.

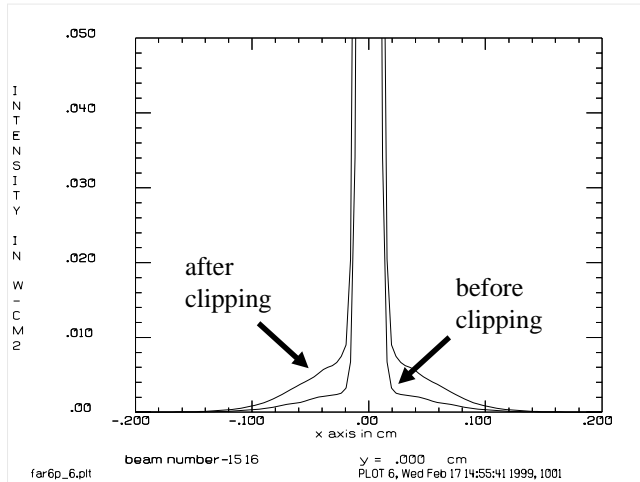


Fig. 16. Non-gaussian speckle. Comparison of time-averaged autocorrelation function for the speckle before and after rear aperture conditioning. Function is shown from 0 to .05 relative intensity to better display the side lobe structure that is formed by the aperture clipping. These autocorrelation functions were evaluated over the entire  $.4 \times .4$  cm aperture. Both the envelope in the near-field and the rear aperture clipping render the speckle somewhat nongaussian.

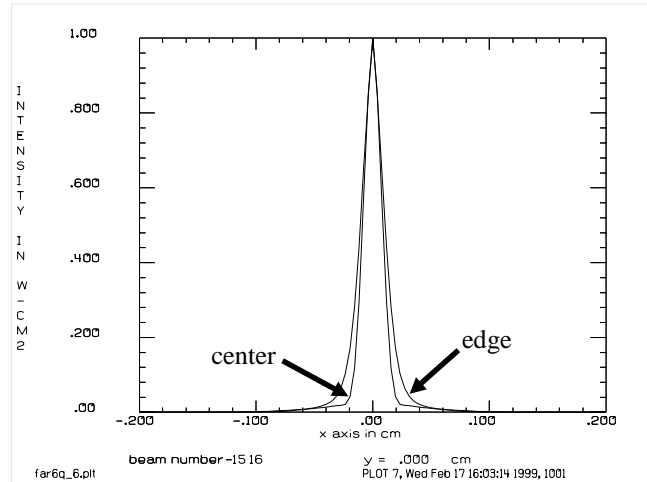


Fig. 17. Non-stationarity of speckle. The autocorrelation after edge clipping was measured in a centered 0.2 cm diameter aperture (narrow function) and the same aperture decentered by 0.2 cm to measure the autocorrelation function near the edge (wide function). The speckle near the edge of the distribution is more affected by the clipping aperture and is correspondingly broadened. The clipping makes the speckle distribution somewhat non-stationary in shape and width.

2. Reinhard Voelkel; Hans P. Herzig, Philippe Nussbaum, Rene Daendliker, William B. Hogle, "Microlens array imaging system for photolithography", *Optical Engineering*, 35, 3323-3330 (1996).
3. L. G. Nazarova, "Measurement of the degree of laser coherence by Young's method," UDC 621.375.9:535,403-405 (1970).
4. J. C. Wyant, "Double frequency grating lateral shear interferometer," *Appl. Opt.* 12, 2057-2060 (1973).
5. Z. B. Liu, J. P. Xie, K. Kuroda, and I. Ogura, "Holographic double frequency grating shearing interferometer and its application to measurement of spatial coherence," *Seisan Kenkyu* 36, 192-194 (1984).
6. Z. Karny, S. Lavi, and O. Kafri, "Direct determination of the number of transverse modes of a light beam," *Opt. Lett.* 8,409-411 (1983).
7. J. Goodman, *Statistical Optics*, John Wiley & Sons (1985).
8. M. Born and E. Wolf, *Principles of Optics*, 6th Edition, Pergamon Press (1980).
9. Shintaro Kawata, Ikuo Hikima, Yukata Ichihara, and Shuntaro Watanabe, "Spatial coherence of KrF excimer lasers," *Appl. Opt.* 31,387-396 (1992).
10. J. Goodman, *Introduction to Fourier Optics*, McGraw-Hill (1968).
11. E. A. Sziklas and A. E. Siegman, "Diffraction calculations using fast Fourier transform methods," *Proc. IEEE* 62, p 410-412 (1974).
12. Anthony E. Siegman and Steven W. Townsend, "Output beam propagation and beam quality from a multimode stable-cavity laser," *IEEE Journal of Quan. Electronics*, Vol. 29, p 1212-1217 (1993).

13. David L. Wright and Steven Guggenheimer, "Status of ISO/TC 172/SC9/WG1 on standardization of the measurement of beam widths, beam divergence, and propagation factor," Proc. SPIE, Vol. 1834, 2-17 (1992).
14. Calculations were performed on a Compaq dual Pentium II 300 MHz computer.
15. GLAD is a commercial program for laser and physical optics propagation. Applied Optics Research, www.aor.com.
16. Uday K. Sengupta, "Krypton fluoride excimer laser for advanced microlithography," Optical Engineering, 32, 2410-2420 (1993).
17. Richard G. Morton, Igor Fomenkov, William Partlo, Palash Das, Richard Sandstrom, "Design considerations and performance of 1 kHz KrF excimer lasers for DUV lithography," SPIE Proceedings, Vol. 2726, p. 900-909, Optical Microlithography IX, Gene E. Fuller Ed. (1996).

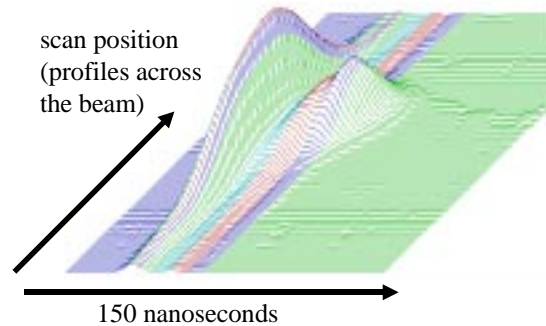
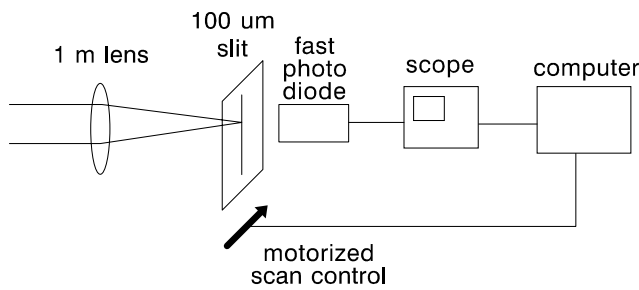


Fig. 18. Schematic to observe time-resolved irradiance profiles. The intensity vs. time is recorded for a particular position of the slit for a series of pulses. Observations may be made at the plane of the lens, at the focal plane of the lens (as shown above), or at other points in the beam.

Fig. 19. The irradiance of a pulse is shown as profiles across the beam as a function of time (x-axis). This laser is emitting a two-step pulse with the first step being wider than the second.

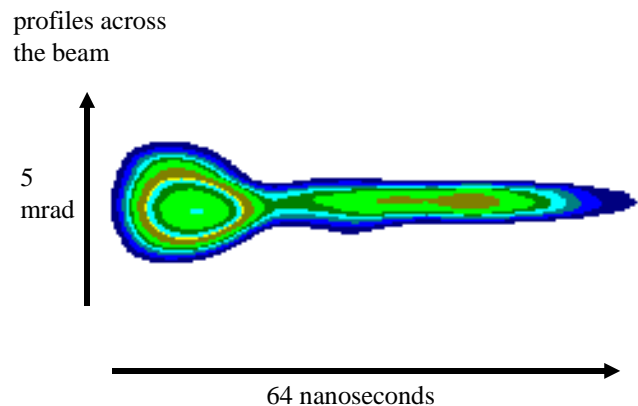
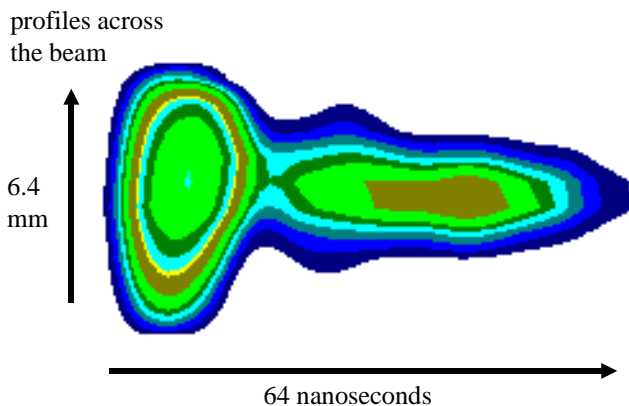


Fig. 20. Near-field. Contour maps of near-field intensity profiles (y-axis) vs. time (x-axis) showing two-step pulse.

Fig. 21. Focal plane of lens. Intensity profiles (y-axis) vs. time (x-axis) showing two-step pulse.